Synthesis, Characterization, and Application of Tunable Resistance Coatings Prepared by Atomic Layer Deposition

Jeffrey W. Elam[a], Anil U. Mane[a], Joseph A. Libera[a], John N. Hryn[a], Oswald H. W. Siegmund[b], Jason McPhate[b], Matthew J. Wetstein[c], Andrey Elagin[c], Michael J. Minot[d], Aileen O'Mahony[d], Robert G. Wagner[a], William M. Tong[e], Alan D. Brodie[e], Mark A. McCord[e], and Christopher F. Bevis[e]

[a]Argonne National Laboratory, Argonne, Illinois 60439, USA
[b]Space Sciences Laboratory, University of California, Berkeley, California 94720, USA
[c]Enrico Fermi Institute, University of Chicago, Chicago, Illinois 60637, USA
[d]Incom, Inc., Charlton, MA 01507, USA
[e]REBL program, Office of the CTO, KLA-Tencor Corp., Milpitas, CA 95035, USA

We describe the synthesis, characterization, and application of nanocomposite, tunable resistance coatings consisting of conducting, metallic nanoparticles embedded in an amorphous dielectric matrix. These films are comprised of $M:Al_2O_3$ with M=Mo or W, and are prepared by atomic layer deposition (ALD) using alternating exposures to trimethyl aluminum and H_2O for the Al_2O_3 ALD and alternating MF_6/Si_2H_6 exposures for the metal ALD. By varying the ratio of ALD cycles for the metal and the Al_2O_3 components in the film, we can tune precisely the resistance of these coatings over a very broad range from 10^5-10^{12} Ohm.cm. These films exhibit ohmic behavior and resist breakdown even at high electric fields of 10^7 V/m. Moreover, the self-limiting nature of ALD allows us to grow these films inside of porous substrates and on complex 3D surfaces. As a result of these qualities, our nanocomposite films have proved exceptional as resistive coatings in microchannel plate electron multipliers and as charge drain coatings in electron-optical devices.

Introduction

Nanocomposite coatings, comprised of an intimately blended mixture of components, have diverse applications in microelectronics, optics, sensors, and solid state detectors. By varying the composition of the mixture, the electrical, optical, and physical properties of the nanocomposite coatings can often be tuned over the full range of the individual components, and can sometimes yield unique properties distinct from either of the constituents. Of the many techniques for producing nanocomposite coatings, atomic layer deposition (ALD) is particularly appealing. ALD uses alternating exposures between gaseous precursors and a solid surface to deposit materials in an atomic layer-by-layer fashion (1). Because the surface chemical reactions naturally terminate when the surface functional groups become consumed, the amount of material deposited in one ALD cycle is easily controlled. This self-limiting property, coupled with facile diffusion of the precursor vapors into narrow pores and voids, allow complex, 3D substrates to be coated with excellent uniformity and conformality (2). A rich variety of materials can be deposited by ALD including metal oxides, nitrides, and sulfides, as well as pure

elements. By alternating between the ALD chemistries for two materials (e.g., a metal and a metal oxide), we can synthesize nanocomposite coatings (3-5). The thickness of the coating is controlled by the total number of ALD cycles performed, and the composition is dictated by the ratio of the ALD cycles executed for the two components.

In this study, we employed *in situ* quartz crystal microbalance (QCM) measurements and Fourier transform infrared (FTIR) absorption spectroscopy to understand the ALD growth mechanism for nanocomposite films comprised of both $Mo:Al_2O_3$ and $W:Al_2O_3$. These films were prepared using alternating exposures to trimethyl aluminum (TMA) and H_2O for the Al_2O_3 ALD, and alternating MF_6/Si_2H_6 exposures for the metal ALD, where M=Mo or W. In the case of the $Mo:Al_2O_3$ films, QCM showed that the Mo ALD inhibits the Al_2O_3 ALD and vice versa. Despite this inhibition, the relationship between Mo content and Mo cycle percentage was easily controlled. Surprisingly, FTIR revealed that the reducing agent for the Mo is not the Si_2H_6, but rather the TMA exposure from the subsequent Al_2O_3 ALD cycle. Elemental analysis showed that the $M:Al_2O_3$ films are uniform in composition and contain Al, O, and metallic Mo or W as expected, but also include significant F and C. Cross-sectional transmission electron microscopy revealed the film structure to be metallic nanoparticles (~1 nm) embedded in an amorphous Al_2O_3 matrix. We have utilized these nanocomposite coatings to functionalize capillary glass array plates to fabricate large-area microchannel plates (MCPs) suitable for application in large-area photodetectors. In addition, we have applied these films as charge drain coatings in electron-optical micro-systems for a prototype electron beam lithography tool, permitting high resolution electron beam patterns without charging artifacts.

Experimental

The $Mo:Al_2O_3$ and $W:Al_2O_3$ composite film ALD was performed at 200°C in a hot-walled viscous flow ALD reactor (6). This reactor was equipped with a quartz crystal microbalance (QCM) that allowed *in situ* studies of the ALD processes. The TMA (97%, Sigma-Aldrich), deionized H_2O, Si_2H_6 (99.998%, Sigma-Aldrich), MoF_6 (99%, Alfa Aesar), and WF_6 (99.8%, Sigma-Aldrich), precursors were maintained at room temperature. The ultrahigh purity (99.999%) N_2 carrier gas flow was set to 300 sccm, which provided a base pressure of 1.0 Torr in the ALD reaction chamber as measured by a heated Baratron pressure gauge (MKS model 629B). The $Mo:Al_2O_3$ and $W:Al_2O_3$ composite films were deposited on *n*-type Si(100) substrates. Prior to ALD, the substrates were cleaned using a 10 min ultrasonic treatment in acetone. For the Al_2O_3 ALD, TMA and H_2O were alternately pulsed into the N_2 carrier flow with the following timing sequence: 1s TMA dose - 5s purge - 1s H_2O dose - 5s purge. The TMA and H_2O partial pressures during the dosing were 0.2 Torr and 0.3 Torr, respectively. Similarly, the Mo and W ALD used alternating exposures to MoF_6/Si_2H_6 and WF_6/Si_2H_6, respectively, with the timing sequence: 1s Si_2H_6 dose - 5s purge - 1s MoF_6 or WF_6 dose - 5s purge, and partial pressures of 0.25 Torr, 0.05 Torr, and 0.05 Torr for the Si_2H_6, MoF_6, and WF_6, respectively. These conditions for the Al_2O_3, Mo, and W ALD provided self-limiting growth as verified by *in situ* QCM measurements.

In situ QCM was performed to examine the $Mo:Al_2O_3$ and $W:Al_2O_3$ composite ALD using different ALD pulse sequences. The QCM measurements typically used 10s N_2 purge times to allow the QCM signal to stabilize after each precursor exposure. Transmission electron microscopy (TEM) analysis was performed by Evans Analytical

Group (Sunnyvale, CA). TEM samples were prepared using the *in situ* FIB lift out technique on an FEI Strata Dual Beam FIB/SEM. The samples were capped with a protective layer of carbon prior to FIB milling, and were imaged with a FEI Tecnai TF-20 FEG/TEM operated at 200 kV in bright-field (BF) TEM mode, high-resolution (HR) TEM mode, and nano-beam diffraction (NBD) mode. The composition of the $Mo:Al_2O_3$ and $W:Al_2O_3$ composite layers was determined by depth profiling using X-ray photoelectron spectroscopy (XPS, Evans Analytical Group) and Rutherford backscattering spectroscopy (RBS, Evans Analytical Group). The metal content in the composite films was measured using X-ray fluorescence (XRF, Oxford ED2000).

The resistance of the $Mo:Al_2O_3$ and $W:Al_2O_3$ composite layers were determined by performing current-voltage (I-V) measurements using a Keithley Model 6487 current-voltage source. To facilitate I-V measurements on these highly resistive coatings, the films were deposited on insulating substrates with lithographically patterned comb structures comprised of interdigitated Au electrodes with a 2 μm spacing (7). These comb structures provided an 80,000x greater effective contact area, and an equivalent boost in current compared to conventional four-point probe measurements. Additional I-V and electron amplification measurements were performed on $W:Al_2O_3$ layers deposited on high aspect ratio (60:1) borosilicate glass capillary arrays with 20 μm pores fabricated by Incom, Inc. (Charlton, MA). These capillary arrays were also coated with an 8 nm ALD MgO emissive layer to boost the secondary electron coefficient, and both sides were coated with 100 nm evaporated nickel-chromium to provide a low resistance electrical contact.

In situ Fourier transform infrared (FTIR) measurements were performed during the $Mo:Al_2O_3$ ALD using a Nicolet 6700 with a liquid nitrogen-cooled MCT-B detector. For these measurements, the FTIR beam was diverted through CsI windows and into the ALD reactor. The windows were protected by gate valves which were closed during the ALD exposures to prevent deposition on the windows. The FTIR beam was directed through a sample comprised of ZrO_2 nanopowder pressed into a stainless steel grid to enhance the sample surface area and boost the optical absorption (8). Prior to the $Mo:Al_2O_3$ ALD, the ZrO_2 powder was coated using 10 cycles of TMA and H_2O for Al_2O_3 ALD.

Results and Discussion

Growth and Properties of $Mo:Al_2O_3$ Composite Films

Figure 1 shows a schematic of the precursor dosing strategy used to synthesize the $Mo:Al_2O_3$ ALD composite films. Alternating TMA/H_2O exposures are executed to deposit Al_2O_3, and periodically a single Si_2H_6/MoF_6 cycle is performed to introduce the Mo. We define the Mo cycle percentage as: $\%Mo=Mo/(Mo+Al_2O_3)*100$ where Mo and Al_2O_3 are the relative numbers of TMA/H_2O and Si_2H_6/MoF_6 cycles performed,
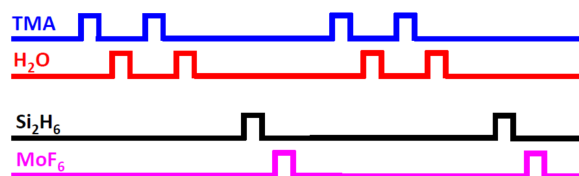
Figure 1: Schematic illustration of precursor pulsing sequence for ALD of $Mo:Al_2O_3$ nanocomposite coating using alternating TMA/H_2O exposures for the Al_2O_3 ALD and alternating MoF_6/Si_2H_6 exposures for the Mo ALD.

respectively. Because of the drastically different resistivities for these two materials ($\sim 10^{16}$ and 10^{-4} Ohm.cm for Al_2O_3 and Mo, respectively), we should be able to tune the resistivity for the composite film over a broad range by adjusting the Mo cycle percentage.

Figure 2a shows *in situ* QCM measurements performed during the ALD of a Mo:Al_2O_3 composite film using a 10% Mo cycle percentage (9 Al_2O_3 ALD cycles followed by 1 Mo ALD cycle). The overall pattern consists of 9 small mass gains followed by a single, larger mass gain, and this pattern is repeated three times in Fig. 2a. Figure 2b shows an expanded view of the boxed region in Fig. 2a and reveals some
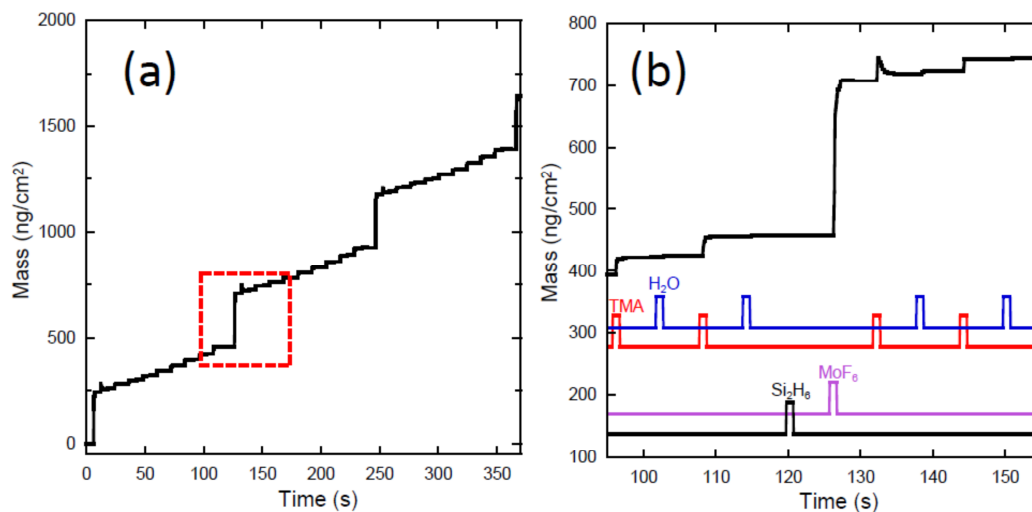
Figure 2: *In situ* QCM measurements during Mo:Al_2O_3 composite film ALD using a 10% Mo cycle percentage (9 Al_2O_3 ALD cycles followed by 1 Mo ALD cycle). (a) Mass vs. time over 30 ALD cycles. (b) Expanded view of the boxed region in Fig. 2a where TMA, H_2O, Si_2H_6, and MoF_6 dose times are indicated at the bottom of the diagram.
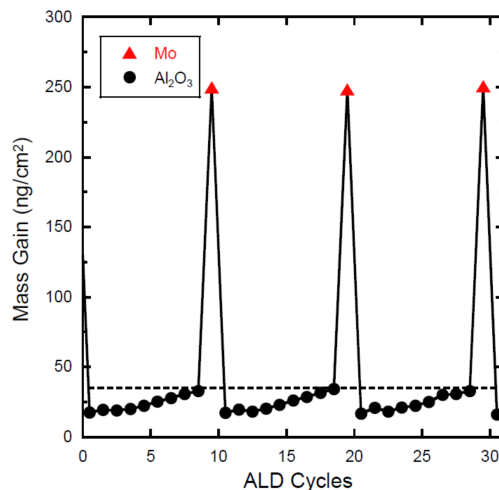
Figure 3: Net mass gains following each ALD cycle of Mo:Al_2O_3 composite film deposition using a 10% Mo cycle percentage. Mo and Al_2O_3 ALD cycles are indicated by the triangles and circles, respectively. The dashed, horizontal line shows the expected steady-state mass gain of 35 ng/cm^2 for Al_2O_3 ALD.

informative details about the QCM mass gains. The TMA, H_2O, Si_2H_6, and MoF_6 dose times are indicated at the bottom of the diagram. Between ~95-115s, two TMA/H_2O cycles for Al_2O_3 ALD are shown and the QCM signals match the expected pattern for Al_2O_3 ALD (3). The net mass gain for each Al_2O_3 ALD cycle is ~30 ng/cm^2, which is slightly smaller than the expected value. In contrast, the QCM signals observed during the Si_2H_6/MoF_6 exposures do not follow the pattern reported in the literature for Mo ALD (9). In particular, no mass gain is observed during the Si_2H_6 exposure, and the net mass gain is only ~250 ng/cm^2, which is far below the 1000 ng/cm^2 expected value for Mo ALD. It is interesting to note that the first TMA exposure following the Mo ALD cycle yields a sharp mass rise followed by a slow decay. This is the signature pattern for a temperature-induced QCM transient produced by an exothermic reaction (10). Figure 3 shows the net mass gains following each ALD cycle for Mo (triangles) and Al_2O_3 (circles). The dashed, horizontal line shows the expected, steady-state mass gains for Al_2O_3 ALD at ~35 ng/cm^2. This figure illustrates that the Al_2O_3 ALD is inhibited by ~50% initially following the Mo ALD, and does not quite achieve the steady-state value even after 9 Al_2O_3 ALD cycles. Moreover, the Mo ALD is also severely inhibited on the Al_2O_3 surface by ~75%.

The origin for some of the unusual QCM results can be gleaned from the *in situ* FTIR measurements. Figure 4 shows the IR absorbance at 4000 cm^{-1} measured following the individual precursor exposures for the Mo:Al_2O_3 composite film ALD, where the precursor pulsed immediately prior to recording the IR spectrum is indicated above each data point. The 4000 cm^{-1} frequency was selected because it falls in a spectral region where there are no peaks from any of the surface functional groups, and therefore serves as an indirect measure of the relative conductivity of the film (11). The IR absorbance at 4000 cm^{-1} remains relatively constant during the TMA and H_2O exposures for Al_2O_3 ALD. We might expect the IR absorbance to increase during the Si_2H_6 exposures for the Mo ALD since Si_2H_6 is believed to be the reducing agent for the Mo (9). However, this is clearly not the case in Fig. 4 which shows practically no changes in the IR absorbance during the Si_2H_6 exposures. Instead, the IR absorbance increases sharply during the TMA exposures that follow the MoF_6 exposures. This finding suggests that TMA is in
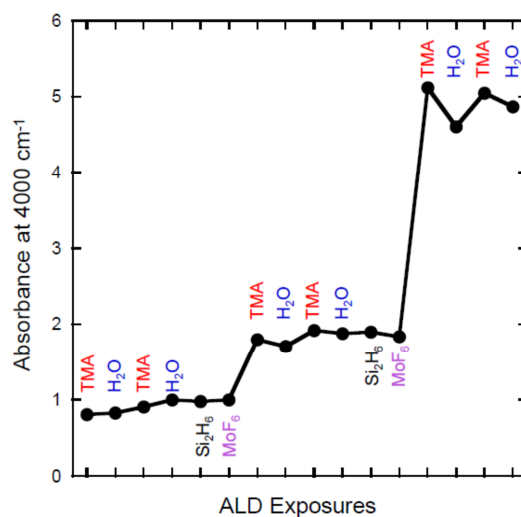
Figure 4: IR absorbance at 4000 cm^{-1} measured by *in situ* FTIR following individual precursor exposures for the Mo:Al_2O_3 composite film ALD. The precursor pulsed immediately prior to recording the IR spectrum is indicated above each data point.

fact the reducing agent, and this idea is consistent with the exothermic transients seen in the QCM data during the TMA exposures following MoF_6 exposures (Fig. 2b). Additional evidence for the reducing effect of TMA on the adsorbed MoF_6 was indicated by a decrease in the $MoOF_x$ stretching frequency at 1040 cm^{-1} during the TMA exposures (not shown).

Figure 5c shows a low resolution cross-sectional TEM image of a 40 nm $Mo:Al_2O_3$ composite film prepared on a Si(100) substrate using 10% Mo cycles. This film appears dense and continuous and the top surface is relatively smooth and parallel to the Si substrate. The interface between the Si substrate and the $Mo:Al_2O_3$ composite film shows a low density, amorphous region attributed to the Si native oxide and Al_2O_3 from the initial ALD cycles. Under higher resolution (Fig. 5a), the $Mo:Al_2O_3$ composite film is seen to consist of 1-2 nm particles (dark spots) embedded in a lower density matrix. Close inspection of the particles (Fig. 5a, inset) reveals weak lattice fringes. Moreover, nano-beam diffraction measurements acquired from the nanocomposite film (Fig. 5b) exhibit diffuse rings consistent with crystalline nanoparticles. Based on these observations, and on our previous study of the $W:Al_2O_3$ composite film ALD (5), we hypothesize that the crystalline nanoparticles in Fig. 5a are metallic molybdenum. These Mo nanoparticles might form through the sintering of Mo atoms upon reduction of $MoOF_x$ surface species by the TMA. The role of TMA as a reducing agent is somewhat surprising, but we believe this to be true based on our FTIR results, and because the microstructure and properties of the $Mo:Al_2O_3$ composite films are practically identical when the Si_2H_6 exposures are not performed.
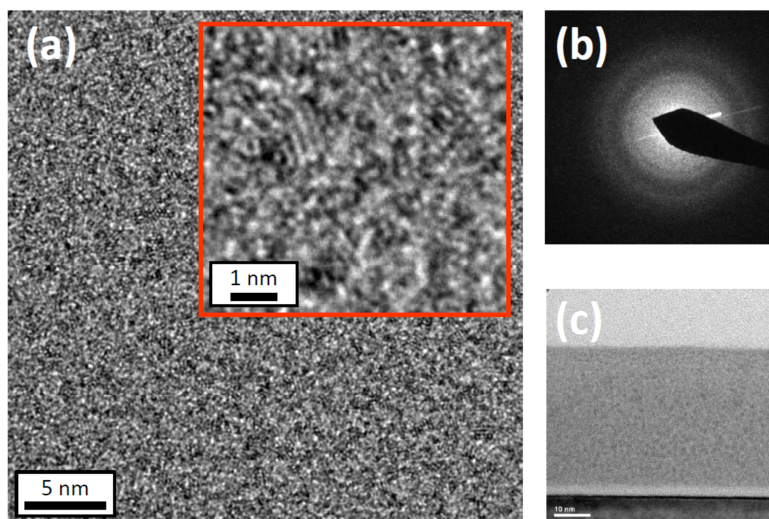
Figure 5: Cross-sectional TEM analysis of 40 nm $Mo:Al_2O_3$ composite film prepared on Si(100) substrate using 10% Mo cycles. (a) High resolution image showing 1-2 nm particles (dark spots) embedded in a lower density matrix. (b) Nano-beam diffraction of film region shown in Fig. 5a. (c) Low resolution image of entire film thickness.

The composition of the $Mo:Al_2O_3$ composite films was determined using XPS depth profiling and RBS measurements of films prepared on Si(100) substrates. These measurements revealed that the films contained Al, O, and Mo as expected, but also contained ~5% C and ~10% F. XPS demonstrated that the Mo exists in both the metallic and sub-oxide (Mo^{+4}) states in the film. These findings, when combined with the QCM and FTIR measurements, suggest that the TMA reduces the adsorbed $MoOF_x$ species to

form AlF$_3$ and metallic Mo. In addition, the C and F presence in the films is similar to that in a previous study which concluded that alternating exposures to niobium pentafluoride and TMA produced films comprised of NbF$_x$, NbC, C, and AlF$_3$ (12).

Next, a series of Mo:Al$_2$O$_3$ composite films was prepared on Si(100) substrates using different Mo cycle percentages and subsequently analyzed by X-ray fluorescence to determine the Mo content of the films. As shown in Fig. 6a, the Mo content increases linearly between 2.1 and 9.0 mol% Mo as the Mo cycle percentage increases from 8 to 15% Mo cycles. This linear relationship demonstrates that the Mo content can be easily and precisely controlled by adjusting the Mo cycle percentage during the Mo:Al$_2$O$_3$ composite film ALD. The resistivity of the Mo:Al$_2$O$_3$ composite films was determined using current-voltage measurements of films deposited on comb structures, and the results are shown in Fig. 6b. Figure 6b shows that the resistivity of the Mo:Al$_2$O$_3$ composite films can be tuned over a very broad, 6-decade range by adjusting the Mo cycle percentage. The range of resistivity values provided by these coatings ($\sim$10^4-10^{10} Ohm cm) is particularly useful for applications in electron multipliers and charge drain coatings, and this capability will be demonstrated below.
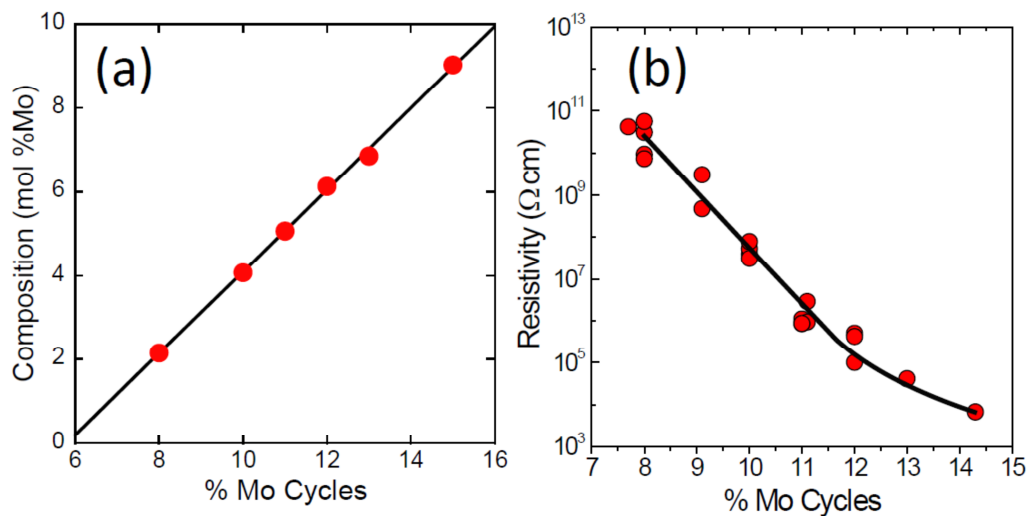
Figure 6: (a) Mo content of ALD Mo:Al$_2$O$_3$ composite films as determined by XRF measurements versus Mo cycle percentage. (b) Resistivity of ALD Mo:Al$_2$O$_3$ composite films as determined by current-voltage measurements versus Mo cycle percentage.

Growth and Properties of W:Al$_2$O$_3$ Composite Films

We performed *in situ* QCM measurements of the W:Al$_2$O$_3$ composite film ALD to explore the growth behavior of these films. We also deposited and characterized a range of W:Al$_2$O$_3$ composite films while varying the W cycle percentage to determine the thickness, composition, morphology, and microstructure of these films and to establish the effect of W content on resistivity. These studies are detailed in our previous publication (5), and some of the major results are presented in Fig. 7. Figure 7a shows the composition of the W:Al$_2$O$_3$ composite films as determined by *in situ* QCM versus the W cycle percentage. The W mol% varies smoothly over the full range of W cycle percentage, and is approximately linear in the range of 10-30% W cycles. Figure 7b shows the effect of varying the W cycle percentage on the resistivity as determined by

current-voltage measurements of films deposited on comb chips and on capillary glass array substrates. The resistivity decreases approximately exponentially from $\sim 10^{12}$ Ohm-cm at 10 %W cycles to $\sim 10^{8}$ Ohm.cm at 30% W cycles. This behavior is similar to that of the Mo:Al$_2$O$_3$ composite films (Fig. 6b), although the slope is much steeper in the case of the Mo:Al$_2$O$_3$ composite films (6 decades over 4% change in Mo cycles) as compared to the W:Al$_2$O$_3$ composite films (4 decades over 20% change in W cycles). This difference may stem from the much higher deposition rate for the ALD Mo (~ 10 Å/cycle) (9) versus the ALD W (~ 4 Å/cycle) (13) under similar growth conditions, especially in light of the exponential relationship between resistivity and metal content.
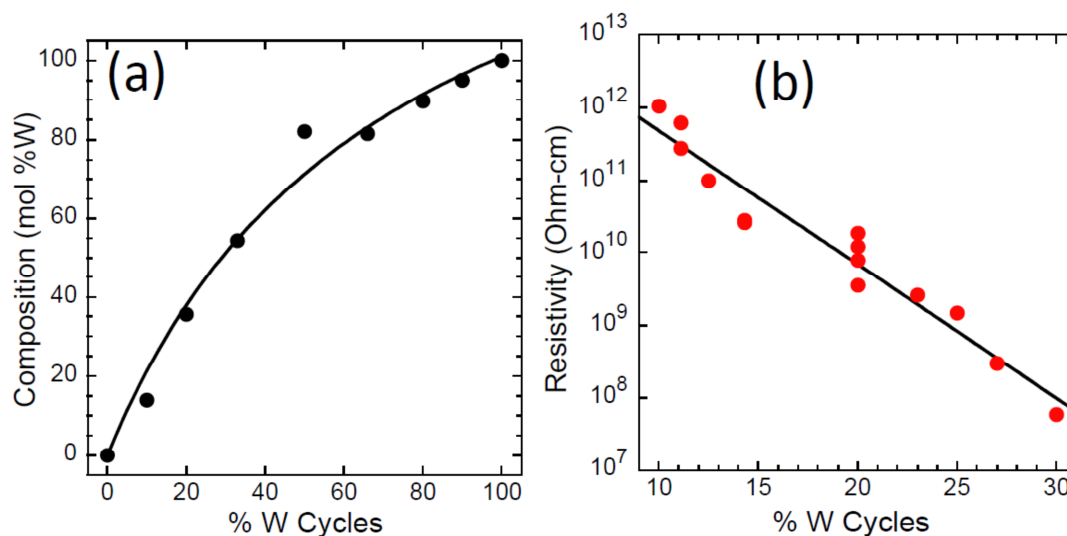
Figure 7: (a) W content of ALD W:Al$_2$O$_3$ composite films deduced from *in situ* QCM versus W cycle percentage. (b) Resistivity of ALD W:Al$_2$O$_3$ composite films determined by current-voltage measurements versus W cycle percentage.

<u>Applications for Tunable Resistance Coatings</u>

A) Microchannel Plates (MCPs)

Microchannel plates (MCPs) are solid-state electron amplifiers comprised of a two-dimensional array of microscopic channels in the form of a thin, flat plate. MCPs are used in detectors to identify low levels of electrons, ions, photons, or neutrons, and provide an amplified response via gain from secondary electron emission that occurs within the individual channels of the MCP (14). This unique quality provides MCPs with the capability to form images, and is critical to a wide variety of detectors and devices. Conventional MCP fabrication involves multi-fiber glass working techniques to draw and assemble an array of solid-core fibers into a block. The block is subsequently sliced into thin wafers and the solid cores are chemically etched to form an ordered array of pores comprised of lead silicate glass. Hydrogen firing is then used to activate the channel walls for electron multiplication. One drawback of this process is that the electrical conductivity and the secondary electron emission properties of the MCP cannot be adjusted independently because both of these properties are imparted during the hydrogen firing step. An additional drawback is that the aspect ratio of the pores (ratio of pore length to pore diameter) is limited to ~100 because it is not possible for the chemical

etchant to diffuse into longer pores without dissolving the lead silicate cladding. This limits the gain that can be achieved.

An alternative strategy for MCP manufacturing is to functionalize glass capillary array wafers using ALD to impart the necessary conductivity and secondary emission properties (15,16). This process is illustrated in Fig. 8 for the case of a 1.2 mm thick, 33 mm diameter disc with a pore size of 20 μm (Fig. 8a-c). Figure 8d shows the 33 mm capillary array disc after ALD of a 94 nm Mo:Al_2O_3 composite film to serve as a resistive layer, and an 8 nm ALD MgO to enhance the secondary electron emission of the surface (17). After the ALD, nickel-chromium electrodes were evaporated onto both sides of the disc to generate the MCP shown in Fig. 8e. The ability to tune the resistivity of the ALD composite film allows MCPs to be manufactured over a broad resistance range so as to be optimized for specific detector applications.
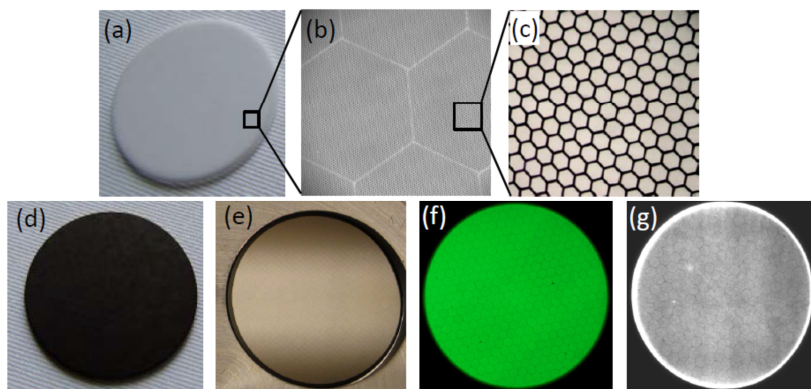
Figure 8: MCP fabrication using ALD tunable resistance coatings. (a-c) 33-mm diameter borosilicate glass capillary array substrate comprised of hexagonal bundles of 20 μm pores. (d) Glass substrate after 94 nm ALD Mo:Al_2O_3 composite resistive layer and 8 nm ALD MgO emissive layer. (e) Completed MCP with nickel-chromium electrodes. (f) Phosphor screen illuminated with electrons amplified by ALD MCP. (g) Gain map for pair of ALD MCPs.
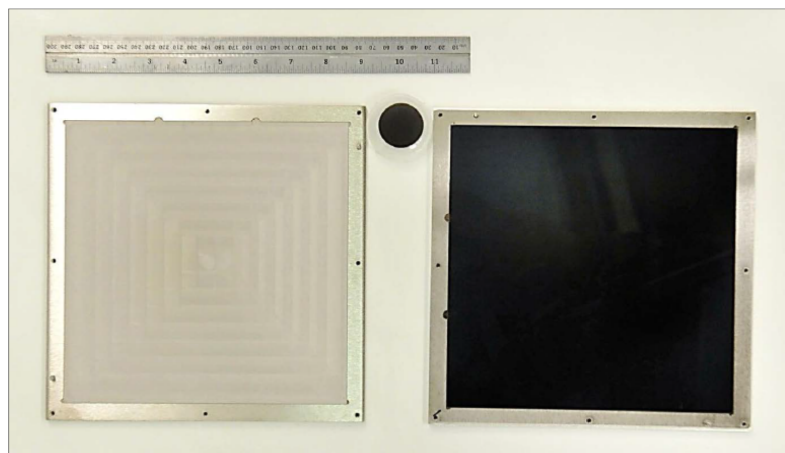
Figure 9: Uncoated 8x8" glass capillary substrate in metal transport case (left) next to identical, 8x8" glass substrate after ALD Mo:Al_2O_3 composite coating. Ruler and 33 mm MCP are shown for scale.

The fully functionalized MCP shown in Fig. 8e was evaluated in a high vacuum system equipped with a calibrated electron source and a phosphor screen to determine the gain and spatial uniformity. As shown by the photograph of the phosphor screen image in Fig. 8f, the MCP response is uniform across the surface. Next, a pair of identical MCPs was assembled in series and installed in front of a position sensitive anode. Using a photon counting mode and weak ultraviolet illumination, a two-dimensional map of the spatial distribution of the gain was generated (Fig. 8g). Figure 8g demonstrates that the gain is very uniform across the MCP. Additional details regarding the performance of the ALD MPCs can be found in ref. (14).

One of the benefits of ALD for MCP manufacturing is that it facilitates scaling to larger detector sizes as demonstrated in Fig. 9. The dark circular disk in Fig. 9 is the 33-mm MCP described above. To the left of this small MCP is an 8x8" glass capillary array substrate in a metal transport case. To the right is an identical 8x8" plate after ALD functionalization and electrode deposition to produce a large-area MCP. To our knowledge, this is the largest MCP ever produced. Work is underway in the Large Area Picosecond Photodetector Project led by Argonne National Laboratory to implement these MCPs for applications in high energy physics (14,15).

B) Charge Drain Coatings

Electrostatic charging is a challenging problem in electron-optical devices such as mass spectrometers, particle detectors, and micro-electro mechanical systems (MEMS). When stray electrons strike the surfaces of insulating components in a vacuum environment, the electrons become trapped. With no means of draining the accumulated electrostatic charge, which can exceed several kilovolts, the local electric field distorts causing loss of focus, resolution, and timing. Simple conducting or semiconducting films are unsuitable for draining this charge because the high leakage current can exceed the power supply or damage the device through resistive heating. Instead, a thin film with resistivity in the mesoscale (between those of a semiconductor and an insulator, 10^2-10^7 Ohm-cm), is needed. In electron-optical MEMS, the challenge is aggravated by the much closer proximity between the electrons and the surfaces, and the films are subjected to very high electrical fields of up to 25 MV/m. Furthermore, the film must coat all surface orientations while maintaining nanoscale uniformity to ensure equivalent performance across all components.
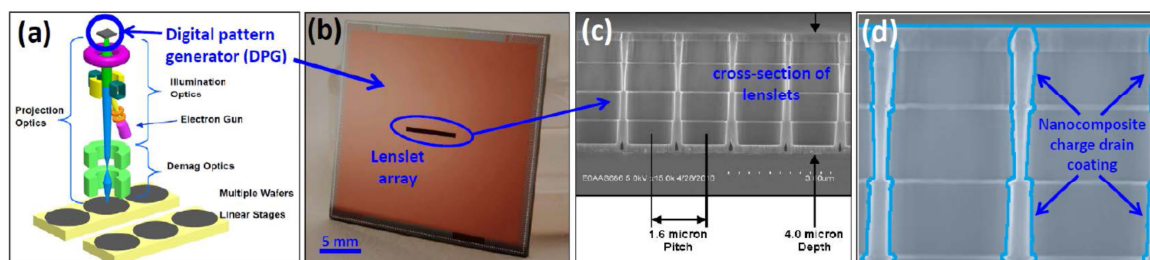
Figure 10: (a) Schematic of KLA-Tencor REBL Nanowriter. (b) REBL digital pattern generator (DPG). (c) Cleaved cross-section of DPG MEMS lenslet array structure. (d) Schematic of ALD charge drain coating covering DPG lenslet array.

The ALD tunable resistance nanocomposite films are an excellent candidate for charge drain coatings. We have demonstrated their benefit in the reflective electron beam lithography (REBL) Nanowriter, a high throughput, direct-writing, maskless lithography tool under development at KLA-Tencor (18). A schematic of the Nanowriter is shown in Figure 10a. The heart of the patterning system is the digital pattern generator (DPG) chip (Fig. 10b). The DPG is an integrated circuit chip with an array of small, independently controllable electron mirrors ("lenslets") producing over 1 million "beamlets". The lenslet electrode MEMS structure is fabricated on top of complementary metal oxide semiconductor (CMOS) circuitry that provides voltage to four electrodes per lenslet to establish the electric fields required to produce an electrostatic lens for each pixel (Fig. 10c). The pixels and lenslets of the array are located on a 1.6-μm pitch, and the lenslet structure is ~4 μm in height. The DPG chip operates under a constant illumination of electrons, and this can lead to electrostatic charging on the insulating oxide surface along the wall of the lenslet vias (Fig. 10c) that reduces the image quality (Fig. 11g). To overcome this problem, the KLA-Tencor DPG chip was coated using an ALD $Mo:Al_2O_3$ composite coating to drain static charge (Fig 10d). Figures 11a-f show images of electron beam test patterns obtained using this DPG. These images indicate virtually defect-free DPG patterns (19).
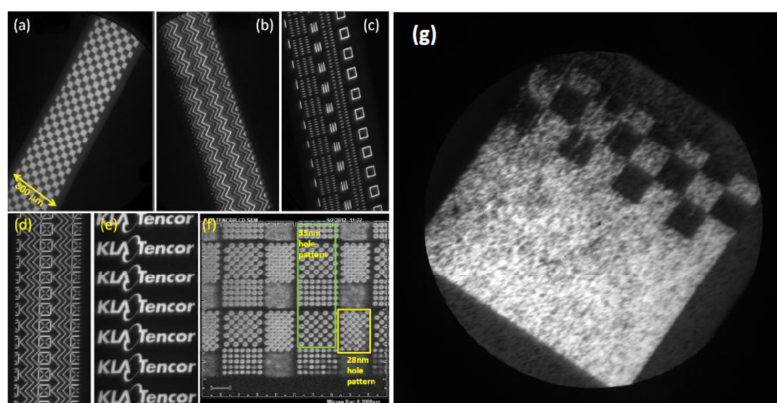
Figure 11: Defect-free test pattern images from DPG coated using ALD $Mo:Al_2O_3$ composite charge drain coating. (a) Square pattern, (b) chevron pattern, (c) stitching pattern, (d) stig test pattern, (e) KLA-Tencor company logo, and (f) contact hole pattern. (g) Poor quality pattern from DPG without ALD $Mo:Al_2O_3$ charge drain coating.

Conclusions

We have developed nanocomposite coatings consisting of conducting, metallic nanoparticles embedded in an amorphous dielectric matrix. These films are comprised of $M:Al_2O_3$ where M= W or Mo, and are prepared by ALD using alternating exposures to TMA and H_2O for the Al_2O_3 ALD, and alternating MF_6/Si_2H_6 exposures for the metal ALD. By varying the ratio of ALD cycles for the metal and the Al_2O_3 components in the film, we can tune precisely the resistance of these coatings over a very broad range from 10^5-10^{12} Ohm-cm. We employed *in situ* QCM and FTIR absorption spectroscopy to understand the ALD growth mechanism for the $Mo:Al_2O_3$ nanocomposite films. These studies demonstrated that TMA serves as the reducing agent to form the conducting Mo. Cross-sectional TEM revealed the film structure to be metallic nanoparticles (1-2 nm)

embedded in an amorphous matrix. We utilized these nanocomposite coatings to functionalize capillary glass array plates to fabricate large-area MCPs suitable for application in large-area photodetectors. In addition, we have applied these films as charge drain coatings in MEMS devices for a prototype electron beam lithography tool, and obtained high resolution electron beam patterns without charging artifacts.

Acknowledgements

References:

1   S. M. George, *Chemical Reviews*, **110**, 1, 111, (2010).
2   J. Elam, 2012, "Coatings on High Aspect Ratio Structures", in *Atomic Layer Deposition of Nanostructured Materials*, edited by N. Pinna and M. Knez (Wiley-VCH, Weinheim), pp. 227.
3   J. W. Elam and S. M. George, *Chemistry of Materials*, **15**, 1020, (2003).
4   J. W. Elam, D. Routkevitch, and S. M. George, *Journal of the Electrochemical Society*, **150**, 6, G339, (2003).
5   A. U. Mane and J. W. Elam, *Chemical Vapor Deposition*, **19**, 4-6, 186, (2013).
6   J. W. Elam, M. D. Groner, and S. M. George, *Review of Scientific Instruments*, **73**, 8, 2981, (2002).
7   A. Brodie, P. De Cecco, C. Bevis, J. R. Maldonado, R. Bhatia, E. Deguns, and G. Sundaram, 2010, "Fabrication of Coatings with Targeted Tunable Electrical Properties via ALD: Al_2O_3/ZnO and Nb_2O_5/Ta_2O_5", in *Atomic Layer Deposition Applications 6*, edited by J. W. Elam, S. DeGendt, O. VanDerStraten, A. Delabie, A. Londergan, S. F. Bent, and F. Roozeboom, Vol. 33, pp. 101.
8   J. D. Ferguson, A. W. Weimer, and S. M. George, *Applied Surface Science*, **162-163**, 280, (2000).
9   D. Seghete, G. B. Rayner, Jr., A. S. Cavanagh, V. R. Anderson, and S. M. George, *Chemistry of Materials*, **23**, 7, 1668, (2011).
10   S. T. Christensen and J. W. Elam, *Chemistry of Materials*, **22**, 8, 2517, (2010).
11   X. Du, Y. Du, and S. M. George, *Journal of Physical Chemistry A*, **112**, 39, 9211, (2008).
12   J. A. Klug, T. Proslier, J. W. Elam, R. E. Cook, J. M. Hiller, H. Claus, N. G. Becker, and M. J. Pellin, *Journal of Physical Chemistry C*, **115**, 50, 25063, (2011).
13   F. H. Fabreguette, Z. A. Sechrist, J. W. Elam, and S. M. George, *Thin Solid Films*, **488**, 1-2, 103, (2005).

14   O. H. W. Siegmund, J. McPhate, A. S. Tremsin, S. R. Jelinsky, H. J. Frisch, J. W. Elam, A. U. Mane, R. G. Wagner, M. J. Minot, J. M. Renaud, and M. A. Detarando, *Physics Procedia*, **37**, 803, (2012).

15   A. U. Mane, Q. Peng, J. W. Elam, D. C. Bennis, C. A. Craven, M. A. Detarando, J. R. Escolas, H. J. Frisch, S. J. Jokela, J. McPhate, M. J. Minot, O. H. W. Siegmund, J. M. Renaud, R. G. Wagner, and M. J. Wetstein, 2012, "An atomic layer deposition method to fabricate economical and robust large area microchannel plates for photodetectors", in *Proceedings of the 2ⁿᵈ International Conference on Technology and Instrumentation in Particle Physics*, edited by T. Liu, Vol. 37, pp. 722.

16   D. R. Beaulieu, D. Gorelikov, H. Klotzsch, P. de Rouffignac, K. Saadatmand, K. Stenton, N. Sullivan, and A. S. Tremsin, *Nuclear Instruments & Methods in Physics Research Section a-Accelerators Spectrometers Detectors and Associated Equipment*, **633**, S59, (2011).

17   S. J. Jokela, I. V. Veryovkin, A. V. Zinovev, J. W. Elam, A. U. Mane, Q. Peng, Z. Insepov, and P. Large Area, 2012, "Secondary electron yield of emissive materials for large-area micro-channel plate detectors: surface composition and film thickness dependencies", in *Proceedings of the 2ⁿᵈ International Conference on Technology and Instrumentation in Particle Physics*, edited by T. Liu, Vol. 37, pp. 740.

18   P. Petric, C. Bevis, M. McCord, A. Carroll, A. Brodie, U. Ummethala, L. Grella, A. Cheung, and R. Freed, *Journal of Vacuum Science & Technology B*, **28**, 6, C6C6, (2010).

19   W. M. Tong, A. D. Brodie, A. U. Mane, S. Fuge, F. Kidwingira, M. A. McCord, C. F. Bevis, and J. W. Elam, *Applied Physics Letters*, **102**, 25, 252901 (5 pp.), (2013).